Single Potassium Niobate Nano/Microsized Particles as Local Mechano-Optical Brownian Probes

Flavio M. Mor,[*,†] Andrzej Sienkiewicz,[†,‡] Arnaud Magrez,[†] László Forró,[†] and Sylvia Jeney[†]

Laboratory of Physics of Complex Matter (LPMC), Ecole Polytechnique Fédérale de Lausanne (EPFL), CH-1015 Lausanne, Switzerland, and ADSresonances, CH-1028 Préverenges, Switzerland

E-mail: flavio.mor@alumni.epfl.ch

Phone: +41 (21) 693 4438. Fax: +41 (21) 693 4470

KEYWORDS: photonic force microscopy, optical trapping, $KNbO_3$ particles, Brownian motion, second-harmonic generation, luminescence energy transfer

SUPPORTING INFORMATION

List of Figures

[*]To whom correspondence should be addressed
[†]Ecole Polytechnique Fédérale de Lausanne
[‡]ADSresonances

Computation of the trap stiffness and estimation of the upper size limit for optically trappable 'cubic-shaped' $KNbO_3$ particles

Both, the geometric ray optics and the Rayleigh approximation provide an easy to understand qualitative pictures of trapping, and useful quantitative results in their respective size regimes. However, many particles in optical trapping lie between these two regimes, and require the use of exact electromagnetic theory to calculate forces. In this intermediate regime the situation at the focus is best described by the Lorentz-Mie theory, which was originally developed to describe scattering of plane waves. The difficulty here is to model the incident wave as a tightly focused beam. The extension of the Lorenz-Mie theory to non-planar illumination is called the generalized Lorenz-Mie theory (GLMT),[1] and is now widely used to model optical trapping of homogeneous isotropic spheres.[2–9]

Even though calculation of the solution of the GLMT requires significant computational effort, methods are well-known and becoming more and more accessible with faster computer and and simulation packages.[10] In order to precisely predict and characterize the forces acting on the optically trapped sphere, we used computational modeling based on a Matlab toolbox recently developed by T. A. Nieminen et al.[10]

The theoretical trap stiffness for each component results from the negative gradient of the computed force. For a linear restoring force along the i-axis, $f_i(i) = -\kappa_{0,i} i$, the trap stiffness is constant in space and given by $\kappa_{0,i}$. The variable $\kappa_{0,i}$ denotes the i-component of the theoretical trap stiffness normalized to the laser power ($i = x, y, z$) at the equilibrium position.

In optical trapping, the refractive index of the medium, n_{f}, imposes a lower limit on the refractive index of a trapped object, e.g. a sphere, with the refractive index n_{s}, through a condition: $n_{\mathrm{s}} - n_{\mathrm{f}} > 0$. Interestingly, also a higher limit for the mismatch of the refractive indices does exist and depends on the sphere size $(2R_{\mathrm{s}})$.

As can be seen in Figure S1a, by applying a simulation procedure based on the GLMT theory, it is possible to examine the possibility of optical trapping for a sphere having a known size, $2R_\mathrm{s}$, and refractive index, n_s. In contrast, determination of the exact sphere size, while knowing its refractive index n_s, is impossible because the axial equilibrium position (i.e. at $x = y = 0$, $z_\mathrm{eq}(0,0)$, diverges close to the exact particle size (Figure S1b, dashed lines).
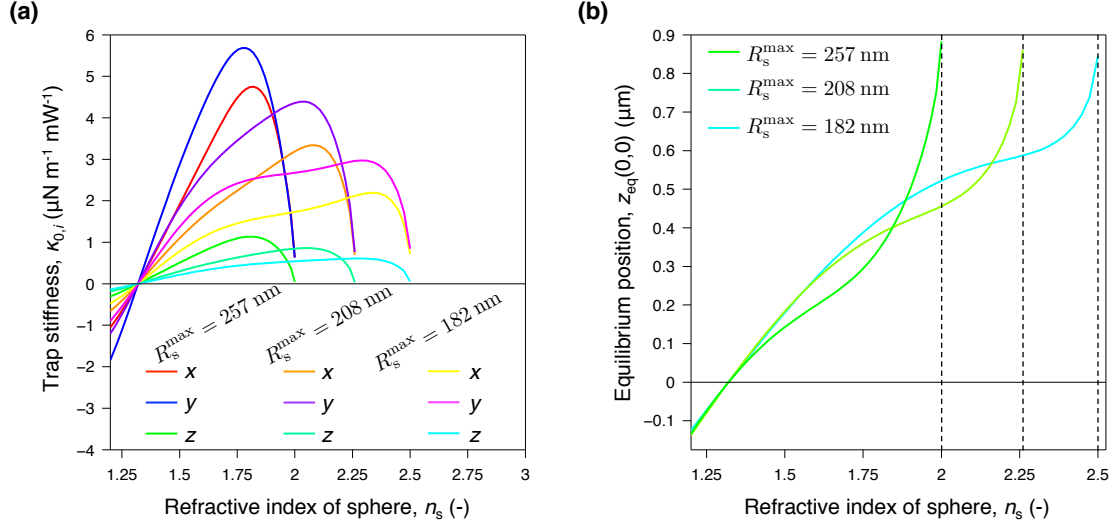

Figure S1: (a) The calculated stiffness of an optical trap for spherical particles immersed in water as a function of the spheres' refractive indices, n_s. The simulation yielded the following maximum sphere radii ($R_\mathrm{s}^{\mathrm{max}}$): 257 nm, 208 nm and 182 nm, for spheres with refractive indices n_s of 2.0, 2.26 and 2.5, respectively. (b) The corresponding calculated axial equilibrium position, $z_\mathrm{eq}(0,0)$, for three optically trapped spheres with radii (R_s): 182 nm, 208 nm and 257 nm, plotted as a function of the sphere's refractive index, n_s.

In particular, as can be seen in Figure S1a, for a refractive index of 2.25, the three components of the trap stiffness converge to zero for a spherical particle with the particle radius $R_\mathrm{s} = 208$ nm. Since, at 1064 nm, the largest component of KNbO$_3$ refractive index (n_z) is of 2.26,[11] we assumed $2R_\mathrm{s} = 416$ nm as the maximum size for a 'cube-shaped' KNbO$_3$ particle that could still be optically trapped in our experimental setup.

Experimental setup

A schematic diagram of the experimental setup is shown in Figure S2. The trapping laser beam was generated by a near-infrared (NIR) laser (IRCL-500-1064-S, CrystaLaser, USA), operating at $\lambda = 1064\,\text{nm}$.

To achieve the optimal trapping efficiency, the NIR laser beam was expanded by a beam expander, EXP (Sill Optics, Germany). If necessary, the intensity of the laser beam could be attenuated by a neutral density filter, NF1 (OWIS, Germany). A polarizing beamsplitter cube, PBS (PBS25-1064-HP, Thorlabs, USA), defined the laser polarization.
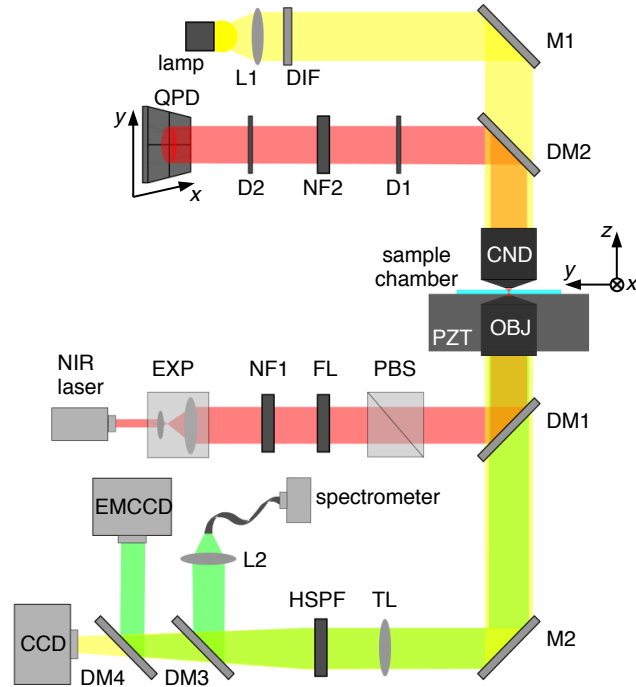

Figure S2: Schematic diagram of the experimental setup. The essential pathways corresponding to the propagation of the NIR light, visible light and SHG emission are depicted by red, yellow and green colors, respectively.

A laser line filter, FL (FL1064-3-∅1, Thorlabs, USA), was used to remove the residual light of the NIR laser pump (operating at 806 nm). The NIR light was then reflected by a first dichroic mirror, DM1 (AHF Analysentechnik AG, Germany), into a high numerical aperture (NA) objective, OBJ (water-immersion, 60x, NA = 1.2, UPLapo/IR, Olympus, Japan). OBJ focused the laser beam down to its diffraction limit onto the object plane of

the microscope, thus creating the optical trap.

To avoid saturation of the quadrant photodetector, QPD (G6849, Hamamatsu Photonics, Japan), a neutral density filter, NF2 (OWIS, Germany), could be placed in front of the QPD, especially when maximal laser powers were used for strong trapping. Two diaphragms, D1 and D2 (OWIS, Germany), were used to align the NIR laser beam (Figure S2, the light pathway depicted in red).

The investigated sample was mounted onto a piezo scanning stage, PZT (P-561, Physik Instrumente, Germany). This allowed achieving three-dimensional (3-D) sample manipulation and positioning, relative to the fixed optical trapping focus. PZT, in combination with a digital controller (E-710.3CD Digital PZT Controller, Physik Instrumente, Germany), had a travel range of 100 μm along all three dimensions (3D), with *ca.* 1-nm movement accuracy. Such a precision was assured through implementation of an electronic feedback circuitry (not shown in Figure S2).

To illuminate the sample with the visible light, a 50-W halogen lamp (OWIS, Germany) was used. Firstly, the visible light was collected by a lens, L1 (Thorlabs, USA). Subsequently, the visible light was diffused by a light diffuser, DIF (OWIS, Germany), reflected by a first mirror, M1 (OWIS, Germany) and projected onto a condenser objective, CND (water-immersion, 63x, NA = 0.9, Achroplan, Zeiss, Germany). After having passed through the investigated sample, the visible light was reflected by a second mirror, M2 (OWIS, Germany), and finally focused by a 300-mm tube lens, TL (Thorlabs, USA), onto a charge-coupled device CCD camera (ORCA ER S5107, Hamamatsu Photonics, Japan). The PZT scanning stage, CCD camera, data acquisition, as well as data analysis and representation were controlled and coordinated by a custom-developed software.

The second-harmonic generation (SHG) light emitted by a trapped particle, after being collected by OBJ, was transmitted by DM1, reflected by M2, transmitted further through TL, reflected by a dichroic mirror, DM3, to be finally focused by a second lens, L2 (Thorlabs, USA), on a fiber optic termination. Then, the SHG emission was delivered to the

photosensitive detector of a spectrometer (USB2000-FL-450, Ocean Optics Inc., USA) via the optical fiber (400 µm in diameter). The spectrometer covered the spectral range from 360 to 1050 nm, with a wavelength resolution of ~ 0.35 nm.

A set of two 50% dichroic mirrors, DM3 and DM4 (Thorlabs, USA), allowed to simultaneously detect the SHG emission spectrum and acquire the 2-D image of its spatial distribution. The latter function was assured by an electron multiplying charge-coupled device, EMCCD, camera (iXonEM+897, Andor Technology, United Kingdom). To achieve the highest quantum efficiency, the EMCCD camera was cooled down to -90 °C, thus reaching a maximum value of 92.5% at 575 nm.

Unlike the Ocean Optics spectrometer, the CCD and EMCCD cameras had to be protected from the backscattered 1064-nm laser beam with a holographic notch filter, HSPF (Kaiser Optical System Inc., USA). Indeed, the maximum wavelength detectable by the Ocean Optics spectrometer was ~ 1053 nm, whereas the CCD and EMCCD cameras were both sensitive up to 1100 nm.

Evaluating the size of KNbO$_3$ nano/microsized particles

It is customarily accepted that SHG intensities for individual spherical particles prepared from non-centrosymmetric materials linearly increase with the squared particle volume, V_p^2.[12,13]

Moreover, according to the GLMT theory for spherical particles, the maximum size $(2R_\mathrm{s}^\mathrm{max})$ of a KNbO$_3$ particle, which could still be optically trapped in our experimental setup, was evaluated to be of 416 nm. Therefore, by a simple rule of proportionality, we could characterize sizes of smaller, 'cube-shaped' particles, exhibiting weaker SHG signals than the reference KNbO$_3$ particle with a size of 416 nm. In particular, for smaller 'cube-shaped' particles this approach yielded the following estimated particle sizes: 298 nm, 340 nm, 380 nm and 400 nm.

The corresponding SHG signals acquired for this set of particles (all with sizes below 416 nm) are shown in Figure 3a (main plot). As can also be seen in Figure 3a (inset), the SHG intensities for this set of particles linearly scales down with diminishing V_{p}^2.

We used the same approach to estimate the approximate size (372 nm in diameter) of the 'cube-shaped' $KNbO_3$ particle, whose SHG signal is compared in Figure 3b (main plot) with the SHG signal emitted by the reference particle having a size of 416 nm.

Quantifying Brownian motion for spheres

The main parameters that can be directly measured in photonic force microscopy (PFM) are the trap stiffness K and the resulting trapping volume probed by the sphere. In order to quantify these parameters in their physical units, the very first step is to calibrate the three position signals, $x^{\mathrm{v}}(t)$, $y^{\mathrm{v}}(t)$ and $z^{\mathrm{v}}(t)$, which are measured in volts by the quadrant photodiode (QPD).

The trap stiffness K has to be determined separately for each dimension as optical traps are usually not perfectly symmetric in the lateral xy-plane and are also very often much softer along the optical z-axis, due to the inherently elongated point spread function. This asymmetry yields a lower resolution, and a higher noise floor in z, which then masks any interesting features in power spectral density PSD_z at high frequency (Figure S3a, green circles). In contrast, K_x and K_y are straightforwardly determined from the functions calibrated according to the procedure described in,[14] as shown in Figure S3a for a 1.14-µm melamine resin sphere trapped at a laser power $P_{\mathrm{laser}} = 6.53\,\mathrm{mW}$. At higher frequencies than 100 kHz, noise becomes too important in PSD_z, but PSD_x and PSD_y can be fitted from 500 kHz to frequencies as low as 1 Hz. In order to overcome the S/N limitation in z, which leads to an unresolvable physical information, the corresponding PSD_z is evaluated in the range between 1 Hz and 50 kHz yielding K_z. As a result, we obtained $K_x = 12.3\,\mathrm{\mu N\,m^{-1}}$, $K_y = 10.5\,\mathrm{\mu N\,m^{-1}}$ and $K_z = 3.07\,\mathrm{\mu N\,m^{-1}}$ assuming the sphere radius $R_{\mathrm{s}} = 570\,\mathrm{nm}$.
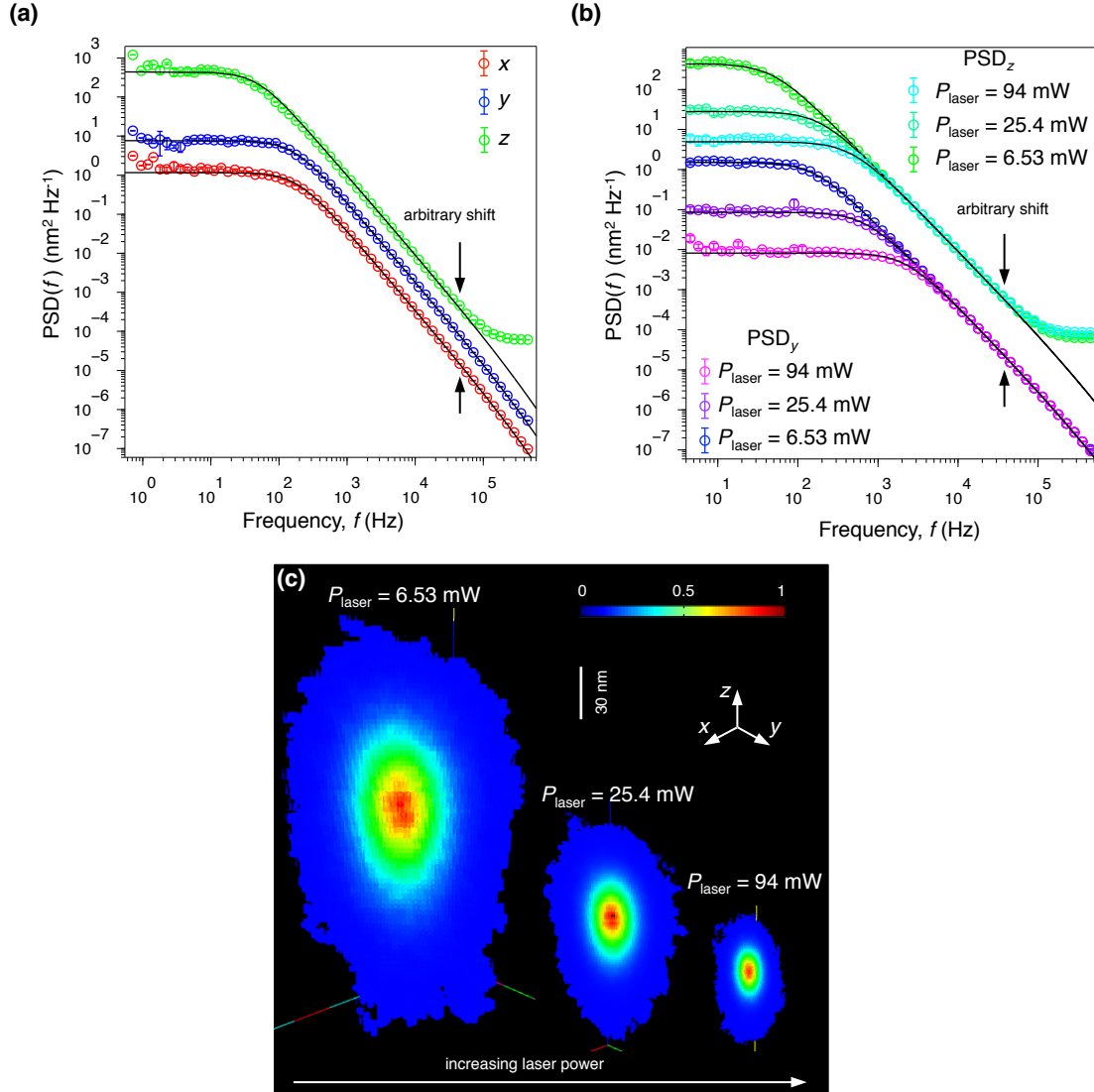
Figure S3: (a) Log-log plot of PSD calibrated along the x-, y- and z-directions for a 1.14-μm melamine resin sphere trapped in water at $P_{\text{laser}} = 6.53$ m W ($\rho_{\text{s}} = 1510$ kg m^{-3}, $\rho_{\text{f}} = 997.6$ kg m^{-3} and $\eta_{\text{f}} = 0.955$ mPa s at $T = 295$ K). The black lines indicate fitting based on the full hydrodynamic theory[14] to all 3D. For clarity, data are arbitrarily shifted along the ordinate by 5 for y and 25 for z and blocked in 10 bins per decade. Error bars give the standard error of the mean from blocking. (b) Effect of P_{laser} on the y- and z-components of PSD. The black lines indicate fitting based on the full hydrodynamic theory.[14] For clarity, the PSDs in z are arbitrarily shifted along the ordinate by a factor of 2. (c) Representation of the corresponding trapping volume at different P_{laser}. The interior of each 3-D sphere's position histogram is visualized using cutting planes. Here, statistic is performed on 100 levels in each direction x, y and z, and all histograms are normalized in intensity (color scale bar) as well as calibrated according to b.

Figure S3b shows the PSD in y and z for three different laser powers P_{laser}, resulting in

three different trap stiffnesses in each dimension. As a result, we obtained $K_x = 50.5 \,\mu\text{N}\,\text{m}^{-1}$, $K_y = 44.3 \,\mu\text{N}\,\text{m}^{-1}$ and $K_z = 12.2 \,\mu\text{N}\,\text{m}^{-1}$, as well as $K_x = 185 \,\mu\text{N}\,\text{m}^{-1}$, $K_y = 144 \,\mu\text{N}\,\text{m}^{-1}$ and $K_z = 29.2 \,\mu\text{N}\,\text{m}^{-1}$, for $P_{\text{laser}} = 25.4 \,\text{mW}$ and $P_{\text{laser}} = 94 \,\text{mW}$, respectively.

The strength of the trap sets the limit of the volume probed by the sphere, which is directly represented by the 3-D position histogram of the center of mass of the sphere. The stronger K_i ($i = x, y, z$) is, the smaller the trapping volume (Figure S3c). In typical cases where $K_x \approx K_y$ and $K_z < K_x$, the position histogram is circular in its xy projection and elongated along the axis z in the xz and yz projections (data not shown).

One-photon excitation of Rose Bengal molecules

To obtain an insight into the evolution of Rose Bengal (RB) fluorescence spectra as a function of concentration under non-standard conditions of two-photon excitation (TPE) in the photonic force microscope (PFM) optical trap, we also acquired RB fluorescence spectra under standard, one-photon excitation (OPE), for the concentrations ranging from 10 to 1000 μM.

It is well established that RB in aqueous solutions aggregates at relatively low concentrations ($\sim 2 \,\mu\text{M}$). The thus formed aggregates are of H-type, absorbing at slightly shorter wavelengths, while emitting at longer wavelengths than the monomers.[15] Additionally, since the emission spectra also depend on self-absorption and concentration-induced quenching, the evolution of the RB fluorescence spectra as a function of concentration is usually complicated and strongly influenced by the experimental conditions.[16] In particular, the variability in the optical path-lengths of the incident and emission radiations strongly modifies the overall evolution of OPE fluorescence spectra of RB.

Therefore, to bring the experimental conditions closer to these used in the PFM, we performed OPE emission measurements by implementing a custom-designed setup that was based on an inverted biological epi-fluorescent microscope (TC5500, Meiji Techno, Japan),

and a spectrofluorometer (USB 2000+XR, Ocean Optics Inc., USA). This setup enabled us to perform fluorescence measurements in flat 0.4-mm thick glass capillaries, thus having the optical path-lengths comparable to that of the PFM sample chamber (0.1 mm).

RB was purchased from Sigma-Aldrich (Switzerland) and used without further purification. Small aliquots of freshly prepared RB solutions ($\sim$ 80 µL) were transferred into rectangle flat borosilicate glass capillary tubes with cross-sectional internal dimensions of 0.4 mm (thickness) and 4.0 mm (width), Model 2540-50, from VitroCom Inc., New Jersey, USA. The OPE fluorescence spectra were acquired using a custom-designed setup based on an inverted biological epi-fluorescent microscope (TC5500, Meiji Techno, Japan), and a spectrofluorometer (USB 2000+XR, Ocean Optics Inc., USA). The fluorescence spectra were recorded upon excitation at $\lambda_{\text{ex}} = 470$ nm. This excitation light was filtered out from the emission of the microscope's Mercury vapor 100-W lamp using a set of Meiji Techno filters, Model 11001v2 Blue.

The amplitude-normalized OPE emission spectra for aqueous solutions of RB, with concentrations ranging from 10 to 1000 µM, are shown in Figure S4. As can be seen, on increasing the concentration of RB, the emission maximum, λ_{em}, shifts to longer wavelengths (inset to Figure S3). This is the expected behavior when aggregation and reabsorption of fluorescence takes place.[16]

Thus, although the optical path-lengths used in OPE and TPE fluorescence detection, being of 0.4 mm and 0.1 mm, respectively, are comparable, the overall concentration-dependent evolutions of the fluorescence emission peak wavelength, λ_{em}, are markedly different for both experiments. The absence of the spectroscopic red-shift in emission spectra upon increasing the concentration of RB in TPE experiments can be associated with several factors, including definitely much smaller active volumes, being only of 0.182 µm^3,[17] probed by a tightly focused laser beam in PFM experiments.
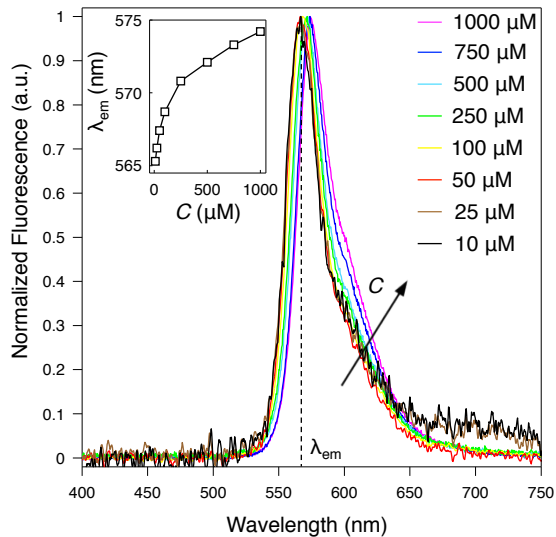
Figure S4: Evolution of RB fluorescence spectra as a function of concentration observed under standard experimental conditions ($\lambda_{\mathrm{ex}} = 470\,\mathrm{nm}$) for concentrations ranging from 10 to 1000 μM. Inset: evolution of the fluorescence emission peak wavelength, λ_{em}, as a function of RB concentration, C.

This alleviates, in part, the influence of self-absorption and concentration-induced quenching, which both depend on the optical path-lengths and contribute to modifications of OPE spectra acquired at standard conditions. Additionally, the selection rules for TPE are different from those of OPE.[18,19] In particular, due to the fact that higher excited singlet states are reached in two-photon experiments, TPE spectra are blue-shifted as reference to fluorescence spectra observed in one-photon experiments.[19,20] This fact might, as well, counterbalance contributions from self-absorption and concentration-induced quenching, which otherwise lead to red-shifted emission spectra for increasing RB concentrations in standard OPE experiments, as it is shown Figure S4.

Laser-induced heating in photonic force microscopy

Laser-induced heating in optical trapping has extensively been discussed by several authors.[21–24] E. J. G. Peterman et al.[23] showed experimentally that for polystyrene or silica microspheres in aqueous solutions, heating was primarily due to the absorption of light by

the fluid, and therefore less dependent on the particle.

Applying the theoretical model developed by E. J. G. Peterman et al.[23] to the experimental conditions used in this work, we expect the temperature increase to be of $\sim 2\,°C$ at the highest laser power of 94 mW (1064 nm) used here.

Even at a trapping wavelength of 980 nm, for which water absorption is known to be higher, and with a 4 times higher laser power, P. Haro-González et al.[24] measured a temperature increase in the solution of maximally 21 K, corresponding to heating of $57\,K\,W^{-1}$.

References

(1) Gouesbet, G.; Grehan, G. *J. Opt.* **1982**, *13*, 97–103.

(2) Ren, K. F.; Gréhan, G.; Gouesbet, G. *Appl. Opt.* **1996**, *35*, 2702–2710.

(3) Wohland, T.; Rosin, A.; Stelzer, E. H. K. *Optik* **1996**, *102*, 181–190.

(4) Maia, N. P. A.; Nussenzweig, H. M. *Europhys. lett.* **2000**, *50*, 702–708.

(5) Mazolli, A.; Maia, N. P. A.; Nussenzeig, H. M. *Proc. R. Soc. Lon. Ser. A* **2003**, *459*, 3021–3041.

(6) Lock, J. A. *Appl. Opt.* **2004**, *43*, 2532–2544.

(7) Lock, J. A. *Appl. Opt.* **2004**, *43*, 2545–2554.

(8) Köner, G.; Parkin, S.; Nieminen, T. A.; Heckenberg, N. R.; Rubinsztein-Dunlop, H. *Phys. Rev. Lett.* **2006**, *97*, 157402–157406.

(9) Neves, A. A. R.; Fontes, A.; de Y. Pozzo, L.; de Thomaz, A. A.; Chillce, E.; Rodriguez, E.; Barbosa, L. C.; Cesar, C. L. *Opt. Express* **2006**, *14*, 13101–13106.

(10) Nieminen, T. A.; Loke, V. L. Y.; Stilgoe, A. B.; Knöner, G.; Branczyk, A. M.; Heckenberg, N. R.; Rubinsztein-Dunlop, H. *J. Opt. A: Pure Appl. Opt.* **2007**, *9*, 196–203.

(11) Umemura, N.; Yoshida, K.; Kato, K. *Appl. Opt.* **1999**, *38*, 991–994.

(12) Joulaud, C.; Mugnier, Y.; Djanta, G.; Dubled, M.; Marty, J.-C.; Galez, C.; Wolf, J.-P.; Bonacina, L.; Dantec, R. L. *Journal of Nanobiotechnology* **2013**, *11*, 1–9.

(13) Mayer, L.; Dantelle, G.; Jacques, V.; Perruchas, S.; Patriarche, G.; Roch, J.-F.; Gacoin, T. *J. Mater. Chem. C* **2014**, *2*, 7681–7686.

(14) Franosch, T.; Grimm, M.; Belushkin, M.; Mor, F. M.; Foffi, G.; Forró, L.; Jeney, S. *Nature* **2011**, *478*, 85–88.

(15) Xu, D.; Neckers, D. C. *J. Photochem. Photobiol. A-Chem.* **1987**, *40*, 361–370.

(16) Martínez-Izquierdo, M. E.; Durand-Alegría, J. S.; Cabrera-Martín, A.; Gallego-Andreu, R. *Analyst* **1984**, *109*, 377–379.

(17) Zipfel, W. R.; Williams, R. M.; Webb, W. W. *Nat. Biotechnol.* **2003**, *21*, 1369–1377.

(18) Xu, C.; Webb, W. W. *J. Opt. Soc. Am. B* **1996**, *13*, 481–491.

(19) Drobizhev, M.; Makarov, N. S.; Tillo, S. E.; Hughes, T. E.; Rebane, A. *Nat. Methods* **2011**, *8*, 393–399.

(20) Hermann, J. P.; Ducuing, J. *Opt. Commun.* **1972**, *6*, 101–105.

(21) Seol, Y.; Carpenter, A. E.; Perkins, T. T. *Opt. Lett.* **2006**, *31*, 2429–2431.

(22) Bendix, P. M.; Nader, S.; Reihani, S.; Oddershede, L. B. *ACS Nano* **2010**, *4*, 2256–2262.

(23) Peterman, E. J. G.; Gittes, F.; Schmidt, C. F. *Biophys. J.* **2003**, *84*, 1308–1316.

(24) Haro-González, P.; del Rosal, B.; Maestro, L. M.; Rodríguez, E. M.; Naccache, R.; Capobianco, J. A.; Dholakia, K.; Solé, J. G.; Jaque, D. *Nanoscale* **2013**, *5*, 12192–12199.